

The Dynamical Environment For The Exploration Of Phobos

By Daniel SCHEERES,¹⁾ Stefaan VAN WAL,¹⁾ and Zubin OLIKARA,¹⁾ and Nicola BARESÌ¹⁾

¹⁾*Smead Department of Aerospace Engineering Sciences, The University of Colorado, Boulder, Colorado, USA*

(Received June 21st, 2017)

The Martian moon Phobos is of great interest for both planetary science and space exploration motivations, and has been the frequent target of space missions and remote observations. However, orbital dynamics in its vicinity are strongly perturbed relative to Keplerian motion, with its extreme environment extending to its surface as well. Thus, to plan and implement missions in the vicinity of and on Phobos will require these considerations be taken into account. We use the latest published models of the Phobos shape and dynamics to characterize its dynamical environment, both in close proximity orbit about the body and for motion across its surface. The results of this study have direct application to any orbital, landing or surface motion mission to this body.

Key Words: Phobos, Astrodynamics, Mars Exploration

1. Introduction

Previous studies of dynamics in the Phobos system have been made, with a few that focus on both orbital and surface motion. Wiesel¹²⁾ presented an analysis of motion in this system using simplified shape model for Phobos. Dobrovolskis²⁾ analyzed motion from the surface and studied its tidal stresses. More recently, Zamaro and Biggs¹⁵⁾ performed a systematic study of the system using both ellipsoidal and shape-based models. In our study we consider both surface motion issues and orbital stability issues. We start with a discussion of the base model used throughout the paper. Then we consider the surface force environment and dynamical constraints for motion on the surface. Following this we consider orbital motion about Phobos, both neglecting and accounting for the small eccentricity of Phobos' orbit.

2. Model for Motion in the Phobos System

2.1. Phobos Shape and Gravity Model

Recent camera images with a resolution of approximately 100 m/px taken by the Mars Express spacecraft enabled the development of a higher-resolution shape model. Willner et al. used these images to construct a degree 45 spherical harmonic model of Phobos, which captures significant surface detail and provides a continuous shape representation.¹⁴⁾ In this model, the radius ρ of a surface point is expressed using Fourier series function of its latitude λ and longitude ϕ , as:

$$\rho(\phi, \lambda) = \sum_{j=0}^J \sum_{k=0}^j (A_{jk} \cdot \cos(k\lambda) + B_{jk} \cdot \sin(k\lambda)) \cdot P_{jk}(\sin \phi) \quad (1)$$

where A_{jk} and B_{jk} are the degree j and order k spherical harmonic coefficients, P_{jk} is the corresponding associated Legendre function, and J is the maximum degree of the considered shape model. On the left side of Fig. 1, we show the Phobos shape that is constructed using this model.

The gravitational field of a spherical harmonic shape can be evaluated using a series expansion similar to that of Eq. 1. Unfortunately, this series diverges when evaluated inside of the circumscribing sphere of the considered shape. In order to study

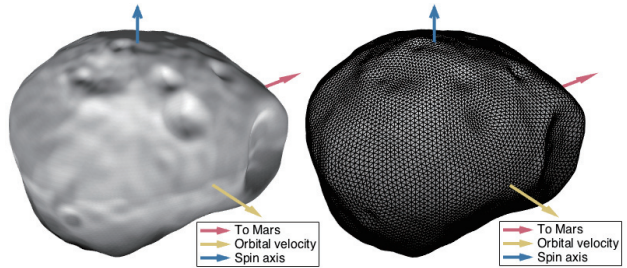


Fig. 1. (left) Degree and order 45 spherical harmonics and (right) polyhedron shape model of Phobos.

the surface dynamics of a body, for which gravity field evaluations on the surface are necessary, we therefore cannot use spherical harmonics for gravitational computations. Instead, we make use of the constant-density polyhedron model, as developed by Werner and Scheeres.¹¹⁾ This model can be evaluated both inside and outside of the circumscribing sphere of a body, and is therefore well-suited to perform gravity field evaluations on the surface. We construct the polyhedron-equivalent of Phobos' spherical harmonic shape by tessellating the shape model such that the resulting polyhedron has $n = 2,562$ vertices; this model is shown on the right-hand side of Fig. 1. By combining the computed volume of this polyhedron and the total mass of Phobos $M = 10,678 \times 10^9$ kg, the corresponding polyhedron density is computed as $\sigma_{poly} = 1.8611$ g/cm³. For comparison, Willner et al. use a bulk density of $\sigma_{sh} = 1.8600$ g/cm³ for Phobos' spherical harmonic shape. With this density value, we can finally evaluate the gravitational potential $U(\mathbf{r})$, acceleration $\nabla U(\mathbf{r})$, and gravity gradient matrix $\nabla \nabla U(\mathbf{r})$ at any position $\mathbf{r} = [x, y, z]^T$ near or on Phobos.

Surface computations are carried out with respect to a Phobos-fixed rotating frame whose positive x -axis points to Mars. The positive z -axis is aligned with Phobos' rotation axis, and the positive y -axis points opposite to Phobos' velocity vector. Although Phobos orbits Mars with a semi-major axis of $a = 9,375$ km and a slight eccentricity of $e = 0.151$,¹³⁾ for surface computations we assume its orbit to be circular, such that the relevant accelerations are invariant along that orbit. The net acceleration experience by a particle with position \mathbf{r} and veloc-

ity $\dot{\mathbf{r}}$ in the Phobos-fixed frame can be expressed as:¹³⁾

$$\ddot{\mathbf{r}} = \nabla U(\mathbf{r}) - \boldsymbol{\omega} \times \boldsymbol{\omega} \times \mathbf{r} - 2\boldsymbol{\omega} \times \dot{\mathbf{r}} + \mu_{Mars} \cdot \left(\frac{\mathbf{r}_{Mars} - \mathbf{r}}{|\mathbf{r}_{Mars} - \mathbf{r}|^3} - \frac{\mathbf{r}_{Mars}}{|\mathbf{r}_{Mars}|^3} \right) \quad (2)$$

where $\boldsymbol{\omega} = \sqrt{\mu_{Mars}/a^3} \cdot \hat{\mathbf{z}}$ is the angular velocity of Phobos, $\mu_{Mars} = 4.2828372854 \times 10^{13} \text{ m}^3/\text{s}^2$ is the gravitational parameter of Mars, and $\mathbf{r}_{Mars} = [a, 0, 0]^T$ is the position vector of Mars (assumed constant) in the Phobos frame.

Eq. 2 has four acceleration terms: the gravitational attraction from Phobos $\nabla U(\mathbf{r})$, centrifugal acceleration $-\boldsymbol{\omega} \times \boldsymbol{\omega} \times \mathbf{r}$, Coriolis acceleration $-2\boldsymbol{\omega} \times \dot{\mathbf{r}}$, and the tidal acceleration from Mars μ_{Mars} . The Coriolis acceleration is zero for stationary particles, which is the case for all further results in this paper, unless explicitly mentioned otherwise. Finally, we note that Eq. 2 corresponds to the acceleration of a particle in the restricted three-body problem (CR3BP), though the gravitational field of the secondary body is not restricted to that of a point mass.

2.2. Hill Approximation

When the Mars-Phobos distance a is much greater than the particle-Phobos distance r , *i.e.*, $a \gg r$, Eq. 2 can be simplified. This results in the famous *Hill* 3-body problem, in which the net particle acceleration is given as:⁸⁾

$$\ddot{\mathbf{r}} = \omega^2 \begin{bmatrix} 3x \\ 0 \\ -z \end{bmatrix} + \omega \begin{bmatrix} 2\dot{y} \\ -2\dot{x} \\ 0 \end{bmatrix} + \nabla U(\mathbf{r}) \quad (3)$$

The accuracy of this approximation can be questioned, as Phobos' orbit lies a mere 2.4 Mars radii away from the surface. To quantify the accuracy, we generate distributions of the net surface acceleration across Phobos' surface with both the full and simplified equations. These distributions are shown on latitude-longitude contour plots in Fig. 2, together with the relative difference between the two expressions. Inspecting this figure, we find that the two expressions are indeed in very close agreement, with the largest error at the sub-Mars point at 0.08%. This allows us to use the simplified expression to evaluate the net acceleration on a particle in the Phobos environment.

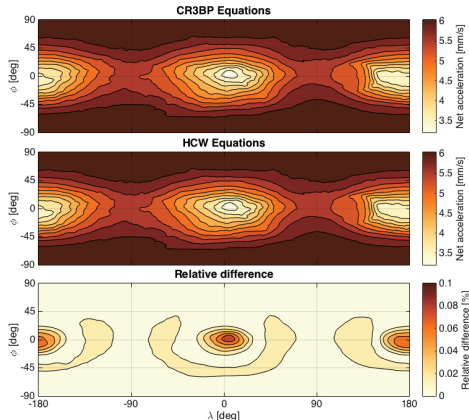


Fig. 2. Net surface acceleration computed with (top) full and (middle) simplified expression, and (bottom) their relative differences.

2.3. Acceleration components

In Fig. 2, we plot the distribution of the net acceleration magnitude across the Phobos surface. In Tab. 1, we provide approximate magnitudes of the separate acceleration components corresponding to Phobos gravity, Mar's gravity, and centripetal

Table 1. Acceleration magnitudes in mm/s^2 .

Acceleration	Poles	Leading/trailing	Sub/anti-Mars
Total	6.3	5.6	3.5
Gravitational	5.8	5.6	5.4
Tidal	0.4	0.6	1.3
Centrifugal	0.0	0.6	0.6

at, respectively, the poles, leading/trailing edges, and sub-/anti-Mars points. Please note that, as the accelerations act in different directions, their magnitudes do not necessarily add up to the magnitude of the total acceleration.

2.4. Surface slope

Using the net acceleration provided by Eq. 3, we can compute the local slope θ across the surface of Phobos, as:

$$\theta = \arccos \left(\frac{\hat{\mathbf{N}} \cdot \ddot{\mathbf{r}}}{\|\ddot{\mathbf{r}}\|} \right) \quad (4)$$

in which $\hat{\mathbf{N}}$ is the surface normal. The resulting slope distribution is included in Fig. 3. We find slopes of up to 35° , though most surface regions have a slope smaller than 15° . As expected, the highest slopes are found on crater rims, particular in Stickney crater. These results match those computed by Willner et al.¹⁴⁾

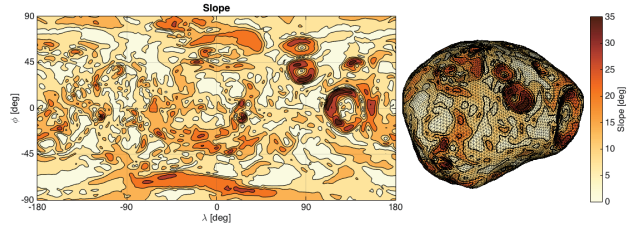


Fig. 3. Slope distribution across the surface of Phobos.

3. Surface Dynamical Environment

Now we consider the characterization of dynamical limits regarding motion on and emanating from the Phobos surface.

3.1. Energy and Velocities

Although the motion of a particle in the Phobos neighborhood does not have any analytical solutions, the three-body motion expressed by Eqs. 2 and 3 does permit one integral of motion that provides insight into the feasible trajectories of a particle. This integral is commonly known as *Jacobi's integral* for the restricted three-body problem. Using our Phobos-fixed frame and the HCW equations and their corresponding assumptions, the integral reduces to a simpler form:

$$C = \frac{1}{2} \omega^2 (3x^2 - z^2) + U(\mathbf{r}) - \frac{1}{2} v^2 \quad (5)$$

This integral, which expresses the total energy of a particle in the Phobos-fixed frame, may be used to study the regions within the three-body system that are accessible to the particle, given some set of initial conditions. By setting $v = 0$ and evaluating Eq. 5 across Phobos' surface, we can determine the the energy distribution of stationary particles on the surface (Fig. 4).

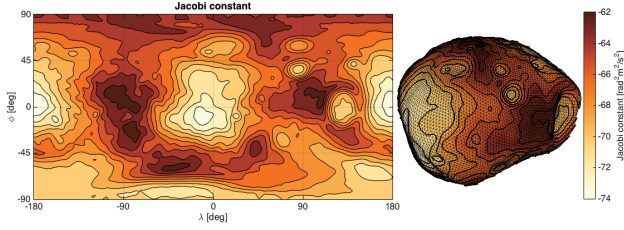


Fig. 4. Jacobi constant distribution across the surface of Phobos.

3.2. Equilibrium points and Roche lobe

The distribution of the Jacobi constant C within the xy -plane of the system is shown in Fig. 5, where we identify two equilibrium points. To compute them precisely we iteratively solve the equation $\nabla C = \mathbf{0}$ to find the L_1 and L_2 equilibrium points,

$$\mathbf{r}_{L_1} = \begin{bmatrix} 17.366 \\ -0.435 \\ -0.322 \end{bmatrix} \text{ km} \quad \text{and} \quad \mathbf{r}_{L_2} = \begin{bmatrix} -17.246 \\ -0.514 \\ -0.096 \end{bmatrix} \text{ km} \quad (6)$$

which have corresponding Jacobi constants C_{L_1} and C_{L_2} .

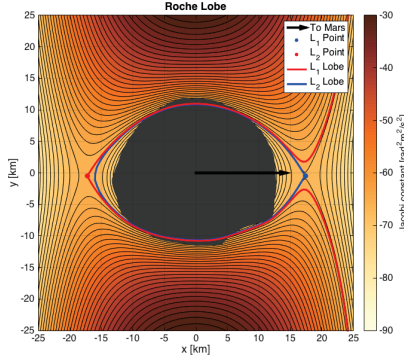


Fig. 5. Zero-velocity curves and Roche lobe of Phobos.

Included in Fig. 5 are also the equipotential lines within the xy -plane that have the same Jacobi constant (and therefore the same energy level) as the L_1 and L_2 points. For the L_1 point, the resulting closed curve is known as the *Roche lobe*. All stationary particles that lie within this lobe are energetically bound to remain in Phobos' vicinity; particles outside of the lobe are not. This means that, energetically, any stationary particle located outside of the Roche lobe could escape Phobos' vicinity through the neck region around L_1 and depart on some orbit that takes it further away from Phobos (return to Phobos is possible, but not guaranteed within finite time). Inspecting Fig. 5, we find that Phobos' leading and trailing edges partially lie outside of this Roche lobe. Particles on these edges are therefore not energetically bound to Phobos, and could escape through the L_1 neck region. A similar curve can be constructed using the energy level of the L_2 point; as the two equilibrium points have highly similar energy levels, the L_1 lobe lies very close to the L_2 Roche lobe. Most particles on the leading/trailing edge therefore also have the energy to escape through L_1 . However, this does not mean those particles have a physical path along which to escape. Indeed, a stationary particle on Phobos' leading/trailing edge would have to burrow through the surface in order to reach either of the neck regions.

3.3. Guaranteed return speed

Stationary particles outside of the L_1 and L_2 lobes have sufficient energy to escape the respective neck regions; particles

within these lobes do not, and are therefore bound to remain within Phobos' vicinity. However, when the latter are given some velocity v , their energy as given by the Jacobi constant C increases, such that the neck regions may open up and allow departure from Phobos. The necessary velocities can be computed from Eq. 5 as:

$$V_i = \begin{cases} \sqrt{2(C - C_{L_i})} & \text{if } C - C_{L_i} > 0 \\ 0 & \text{if } C - C_{L_i} \leq 0 \end{cases} \quad (7)$$

where C is the Jacobi constant of the considered surface location. The velocity V_i is the *guaranteed return speed*, as particles with a velocity lower than V_i cannot pass through the corresponding neck region and escape the Phobos vicinity. Particles with a lower velocity are therefore guaranteed to eventually return to the surface. The surface distributions of V_1 and V_2 are shown in Fig. 6. Following the difference in L_1 and L_2 energy levels, the escape speeds V_2 are slightly higher than the guaranteed return speeds V_1 . We also find that, in addition to the leading and trailing edges, particles on Phobos' northern pole have sufficient energy to escape. This suggests that surface mobility operations are safest when carried out at the sub- and anti-Mars points, and at the southern pole as vehicles operating on these regions do not have sufficient energy to escape Phobos' vicinity. Craft operating on the leading/trailing edges or on the northern pole could escape through either L_1 or L_2 after a small hop, either intentionally or unintentionally.

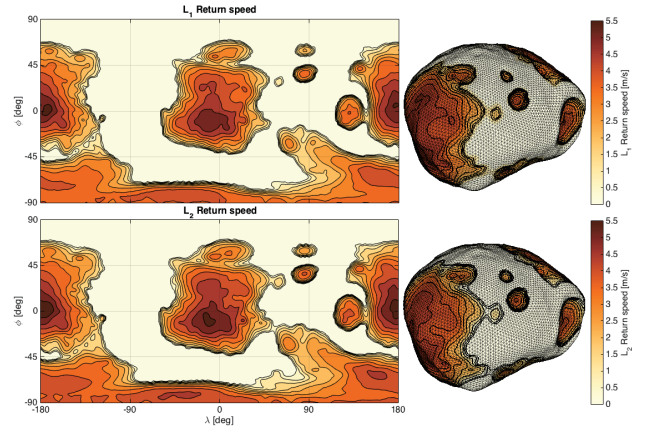


Fig. 6. (top) Guaranteed return speed for (top) the L_1 neck region and (bottom) L_2 neck region.

3.4. Lift-off velocity

The guaranteed return speeds are defined energetically and do not restrict the direction of these velocities; both normal and tangential velocity components are allowed. When we restrict the particle velocity to be purely tangential, a third type of 'speed limit' can be derived that relates to temporary and local lift-off from the surface. This *lift-off velocity* is defined by Van wal and Scheeres⁹ as "the (tangential) surface velocity given to a particle on a body with arbitrary shape, rotation, and gravity, at which the particle will locally lift off from that surface in its direction of travel." It can be expressed as:

$$V_\theta = \pm \sqrt{\rho_\theta^2 (\hat{\mathbf{b}}_\delta \cdot \boldsymbol{\Omega})^2 + \rho_\theta \hat{\mathbf{b}}_\rho \cdot (\tilde{\boldsymbol{\Omega}} \cdot \tilde{\boldsymbol{\Omega}} \cdot \mathbf{P} - \mathbf{a}_E) - \rho_\theta \hat{\mathbf{b}}_\delta \cdot \boldsymbol{\Omega}} \quad (8)$$

where ρ_θ is the surface radius of curvature in the direction of travel $\hat{\mathbf{b}}_\theta$, which governs the magnitude of the lift-off velocity

V_θ . The velocity magnitude therefore varies as a function of the direction of travel, and displays a minimum and maximum that are roughly aligned along and against the local surface rotational velocity. For a detailed discussion of the properties of this expression, and computation strategy for ρ for spherical harmonic shapes, the reader is referred to.⁹⁾

In Fig. 7, we show the surface distribution of minimum and maximum lift-off velocities. Please note that lift-off is only possible when the surface is locally convex; black regions in Fig. 7 are locally concave and are therefore given an infinite lift-off velocity. We find that lift-off is possible in most regions at a velocity of roughly 2 m/s, and is guaranteed in most regions at velocities greater than 8 m/s. In most regions, surface mobility operations can therefore safely be carried out at velocities up to 2 m/s, and should never exceed 8 m/s.

In addition to this lift-off velocity across the curved Phobos surface, we can also develop a lift-off criterion using the local surface normal and net acceleration. This criterion, known as the *ridge* lift-off velocity, expresses the velocity required for a very brief ‘air time’ after an object with finite radius R rolls off a small ridge or asperity on the surface, such as a rock. This velocity is independent of the direction of travel, but does depend on the object radius R , and is equal to:

$$V_R = \sqrt{-R\hat{N} \cdot \ddot{\mathbf{r}}} \quad (9)$$

In Fig. 8, we plot the distribution of the *normalized* ridge lift-off velocity, *i.e.*, of V_R/\sqrt{R} . The values shown therefore also correspond to the ridge lift-off velocity of an object with radius $R = 1$ m. These results show that although an object can move on Phobos’ surface at velocities of several meters per second without lifting off and entering a global ballistic trajectory, we can expect a reduction in friction/traction with the surface at velocities exceeding roughly 7 cm/s due to brief ballistic intervals due to “bumps” on the surface.

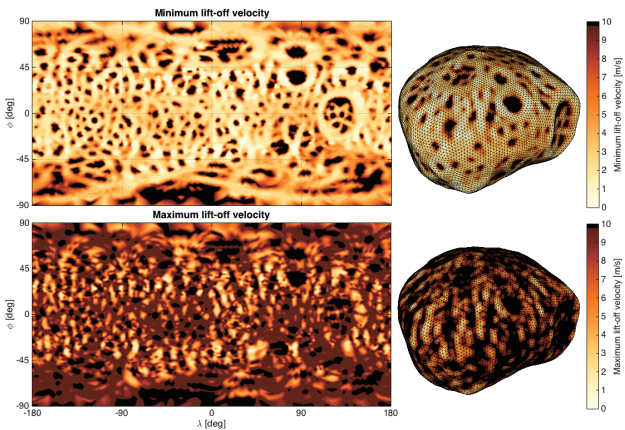


Fig. 7. (top) Minimum and (bottom) maximum lift-off velocity across the surface of Phobos.

4. Orbital Environment

The Phobos orbital environment is now characterized using previously developed methodologies focusing on periodic orbits and their stability. We consider families that both ignore the eccentricity of Phobos’ orbit, and those that account for it.

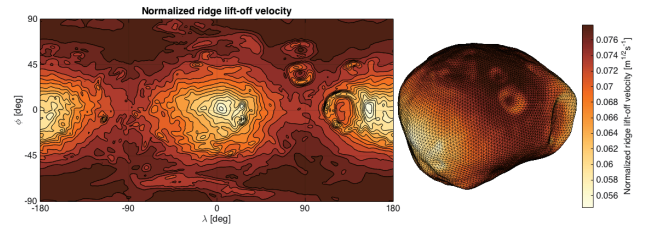


Fig. 8. Normalized ridge lift-off velocity across the surface of Phobos.

4.1. Periodic Orbit Families about the Libration Points

Ignoring the Phobos eccentricity, its shape is fixed in the Hill rotating reference frame allowing us to study the periodic orbits emanating from its libration points. The lack of symmetry of the HR3BP+shape model makes the periodic orbit computation more challenging since the periodic orbit families no longer intersect with each other (except at the equilibrium points where each Floquet multiplier pair corresponds to an emanating family of periodic orbits). Since bifurcations can be quite helpful for exploring periodic orbit families, we start from an intermediate, symmetric model: HR3BP+ellipsoid. That is, instead of using an irregular shape, Phobos is represented as a uniform density tri-axial ellipsoid whose mass and moments of inertia are the same as the polyhedron’s. In all three models (HR3BP, HR3BP+ellipsoid, HR3BP+shape), there are two libration points L1 and L2, though their locations differ between the models. The L1 point lies between Mars and Phobos ($x < 0$ in the plots), and the L2 point is on the far side of Phobos ($x > 0$ in the plots). In all the cases, both libration points have stability (Floquet multiplier pairs) of type: center, center, saddle. As in the usual HR3BP, the two center components in the HR3BP+ellipsoid correspond to planar and vertical periodic orbit families. A notable difference between the HR3BP and the HR3BP+ellipsoid model is that in the latter model the halo orbits bifurcate from the vertical Lyapunov orbits rather than the planar ones. We can, however, take advantage of the fact that our non-symmetric model may be close to a symmetric model. In this case, we can trace out the periodic orbit bifurcation behavior in the symmetric model, then use a homotopy method to move some of these orbits to the non-symmetric model. This way we can obtain orbits in the non-symmetric model that are not directly connected to the equilibrium point. Once we have one orbit on the disconnected branch, we can perform continuation of its family strictly in the non-symmetric model. If the non-symmetric model is far from the symmetric model, completely new branches may also appear that are unrelated to any in the symmetric model.

Periodic orbits related to the libration points in the HR3BP+shape model are shown in Figure 9. Here the planar orbits shown in green have a similar structure to the ellipsoid case, except now these orbits have some small out-of-plane component. However, since the shape model is not symmetric, the bifurcation along the vertical orbit family is no longer present. Instead the small vertical orbits merge into southern halo orbits for L1 (red branch), and the small vertical orbits merge into the northern halo orbits for L2 (yellow branch). For L1, the large vertical orbits (blue) merge into the northern halo orbits (yellow); for L2, the large vertical orbits (blue) merge into the southern halo orbits (red). The approximate turning

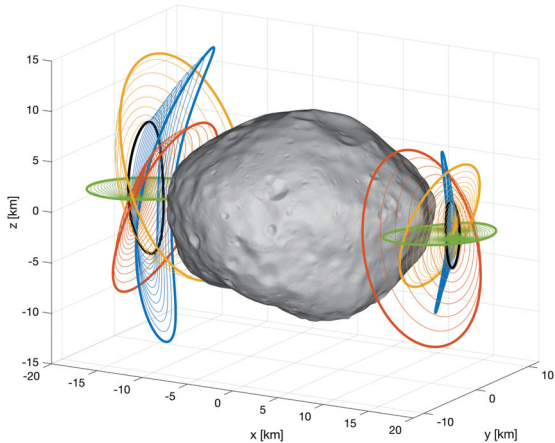


Fig. 9. Periodic orbits for Mars-Phobos HR3BP+shape model.

points are shown as black orbits. Neither of these branches are directly connected to its corresponding libration point. Rather, they were computed by using the homotopy method to move a large vertical orbit from the (symmetric) HR3BP+ellipsoid model to the (non-symmetric) HR3BP+shape model. Then, standard pseudo-arclength continuation could be used to generate the entire branch (including going beyond the turning point).

While the rich structure in these periodic orbit families is of interest, we note that they are all unstable orbits in general. Most relevant, we note that the small interval of stable halo orbits that exist in the Hill problem are not present about Phobos. Thus, while these orbit families control the dynamics about these regions of space, they do not have any direct practical use as their instability times are quite short.

4.2. Stable Periodic Orbits about Phobos

Finally, we consider the family of retrograde periodic orbits about Phobos analogous to the stable retrograde in the Hill 3-body problem.⁴⁾ When far from the body, these degenerate into the 2:1 ellipse orbits found in the Clohessy-Wilshire equations. In our case, we compute both the stable family when the eccentricity is zero, and the quasi-periodic orbits that emerge when non-zero eccentricity is considered.

4.2.1. Dynamical Model for an Eccentric Phobos Orbit

When the Phobos eccentricity is accounted for, following an ellipse around Mars with $e = 0.01515$, the equations of motion of the spacecraft can be described by the elliptic Hill Problem Elliptical Hill Problem (EHP),¹⁰⁾ and can be written as a modification of our earlier equations of motion as:

$$\mathbf{r}'' = \frac{1}{1 + e \cos \nu} \begin{bmatrix} 3x \\ 0 \\ -z \end{bmatrix} + \begin{bmatrix} 2y' \\ -2x' \\ 0 \end{bmatrix} + \frac{1}{1 + e \cos \nu} \nabla \bar{U}(\mathbf{r}) \quad (10)$$

where the $'$ indicates a derivative with respect to the Phobos 2-body true anomaly about Mars and the time and length units of Eq. (10) are normalized such that one orbital revolution of Phobos around Mars corresponds to 2π (i.e., $\omega = 1$) and such that the *resonance radius*⁸⁾ $a(\mu/GM)^{1/3}$ is equal to 1 with μ as the gravitational parameter of Phobos, GM as the gravitational parameter of the Red Planet, and a as the semi-major axis of the planetary satellite. $\bar{U}(\mathbf{r})$ represents the potential normalized by these quantities. It is assumed that the effects of Mars' oblateness are negligible, so that the trajectory of Phobos around Mars can be simply described by its two-body dynamics. Finally, ν

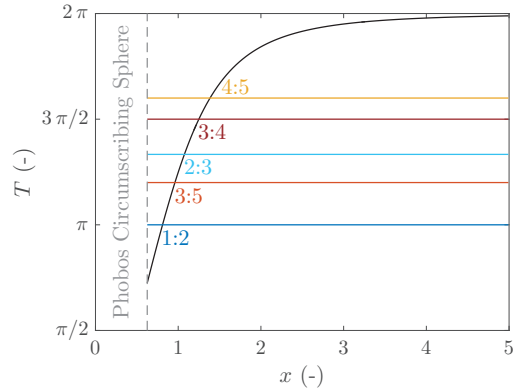


Fig. 10. Period vs positive x -crossing for the family of quasi-satellite orbits with $e = 0$. Only the periodic orbits whose period is resonant with 2π survive when $e \neq 0$.

is the true anomaly of the planetary satellite as well as the independent variable of (10).

It is worth noting that $\nabla \bar{U}(\mathbf{r})$ is obtained from the rotation of the gravitational acceleration computed in Phobos' principal axes frame \mathcal{B} with the algorithm outlined in.¹¹⁾ This accounts for kinematic librations due to the eccentricity of Phobos' orbit. In particular, knowing that Phobos is in a synchronous state and assuming that the principal axes of the small body are oriented such that $\hat{\mathbf{x}}_P$ is pointing towards the anti-Mars direction, $\hat{\mathbf{z}}_P$ is aligned with $\hat{\mathbf{z}}$, and $\hat{\mathbf{y}}_P = \hat{\mathbf{z}}_P \times \hat{\mathbf{x}}_P$, the direction cosine matrix that maps vectors in \mathcal{B} to vectors in \mathcal{S} is given by

$$[\mathcal{S}\mathcal{B}] = \begin{bmatrix} \cos \phi & \sin \phi & 0 \\ -\sin \phi & \cos \phi & 0 \\ 0 & 0 & 1 \end{bmatrix} \quad (11)$$

where the libration angle $\phi = \nu - M$ is equal to the instantaneous difference between ν and Phobos' mean anomaly M .

4.2.2. Periodic Orbits

By inspection of Eq. (10), it is apparent that the equations of motion depend explicitly on the independent variable ν . Consequently, the EHP is a nonautonomous system that does not depend on any external parameter as long as the eccentricity of the planetary satellite is fixed. Following Broucke,¹⁾ this means that periodic orbits are no longer organized in families but are isolated at best. In particular, the period must be resonant with the periodicity of the equations of motion (10), i.e., with the orbital period of Phobos around Mars.

As an example, consider the family of quasi-satellite orbits found in the circular case $e = 0$ when $[\mathcal{S}\mathcal{B}]$ is also equal to the identity matrix. Fig. 10 displays the chart of the periodic orbit period versus the x -axis crossing with $\nu < 0$, illustrating that only those whose period is resonant with 2π actually survive when the eccentricity of Phobos is taken into account.

4.2.3. Quasi-periodic Tori Calculation

As pointed out by Jorba and Villanueva,⁵⁾ quasi-periodic invariant tori of a six-dimensional non-autonomous Hamiltonian system such as (10) lie in one-parameter families. This is equivalent to periodic orbits in the autonomous circular case. As such, quasi-periodic invariant tori should be seen as key players in understanding and organize the dynamics of the EHP. In fact, each of the family members of the QSO family illustrated in Figure 10 gets replaced by a two-dimensional quasi-periodic

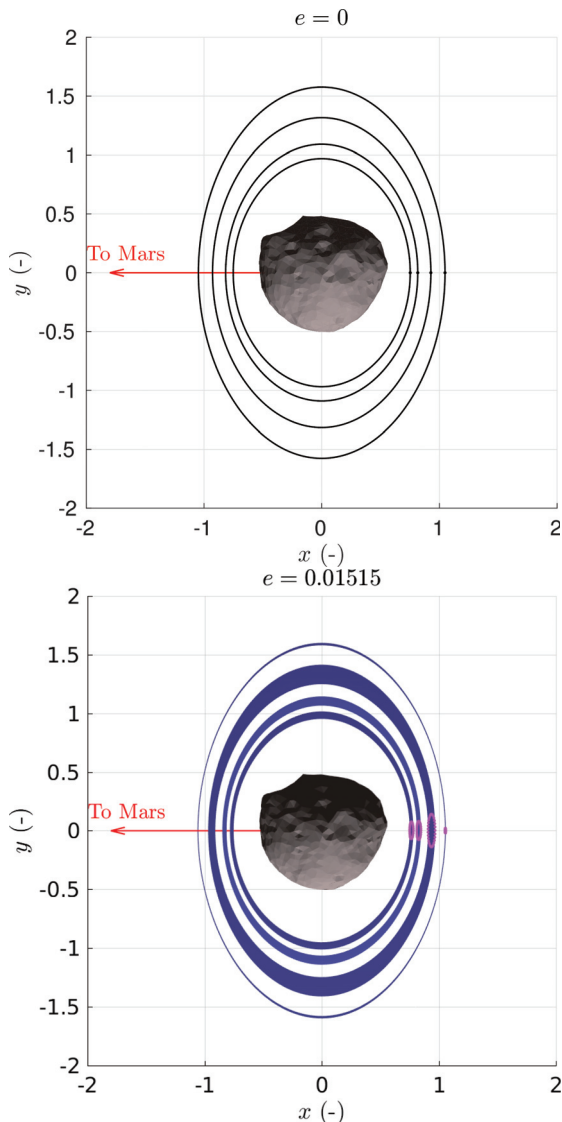


Fig. 11. a) Family of QSO periodic orbits in the circular Hill problem. b) Family of quasi-QSO invariant tori in the elliptic Hill problem. The units in these plots are normalized as described in the text.

invariant torus that belong to a family of quasi-QSO tori.

To compute these invariant manifolds, consider the numerical algorithm outlined in Gómez & Mondelo³⁾ and Olikara & Scheeres⁷⁾ (GMOS). The main idea of the GMOS algorithm is that quasi-periodic invariant tori can be calculated as invariant curves of a stroboscopic mapping by solving a boundary value problem. The interested reader may find more information on the methodology in the PhD. thesis of Olikara.⁶⁾

Some example periodic orbits for the circular case are shown in Fig. 11, top while example quasi-periodic orbits for the eccentric case are shown in the bottom frame. All of these solutions are stable, meaning that perturbations from each of these cases will lie on quasi-periodic orbits in general and just oscillate about the nominal solution. The quasi-periodic orbits shown in the bottom are driven by the periodicity of the Phobos eccentric orbit, and we see that their amplitude grows as they move between the low-order resonances shown in Fig. 10. As the specific resonances are approached, the tori amplitudes shrink until they degenerate into periodic orbits at the

precise resonances, meaning that they lose a dimension. The existence of these stable quasi-periodic orbits in the eccentricity driven case imply that precise mission orbit designs can be flown, with consistent periodic crossing of the two distinct periods distributed about the body.

5. Conclusion

This paper presents and provides a comprehensive analysis of dynamics about and on the surface of the Martian moon Phobos using the best currently available models. The intent of this paper is to provide support for the planning of missions to this body. We find detailed results for surface motion, including limits on the rate of travel on the surface to ensure contact with the surface. For orbital dynamics, we map out the families of orbits in the vicinity of the synchronous orbits about Phobos, noting that their bifurcation structure becomes significantly shifted from the ideal symmetric cases most commonly investigated. Finally, we provide detailed analysis and results for the family of stable retrograde orbits about Phobos, which retain stability up to contact with the surface. When the eccentricity of Phobos is taken into account these orbits expand into quasi-periodic orbits.

Acknowledgments

We acknowledge support from NASA's SSERVI project.

References

- 1) R Broucke. Stability of periodic orbits in the elliptic, restricted three-body problem. *AIAA journal*, 7(6):1003–1009, 1969.
- 2) A.R. Dobrovolskis and J.A. Burns. Life near the Roche limit: Behaviour of ejecta from satellites close to planets. *Icarus*, 42(3):422–441, 1980.
- 3) Gerard Gómez and JOSEP M Mondelo. The dynamics around the collinear equilibrium points of the rtbp. *Physica D: Nonlinear Phenomena*, 157(4):283–321, 2001.
- 4) M. Hénon. Numerical exploration of the restricted problem. V. Hill's case: Periodic orbits and their stability. *Academie des Science Paris Comptes Rendus Serie B Sciences Physiques*, 268:223–238, 1969.
- 5) Angel Jorba and Jordi Villanueva. On the normal behaviour of partially elliptic lower-dimensional tori of hamiltonian systems. *Nonlinearity*, 10(4):783, 1997.
- 6) Z. Olikara. *Computation Of Quasi-Periodic Tori And Heteroclinic Connections In Astrodynamics Using Collocation Techniques*. PhD thesis, University of Colorado, 2016.
- 7) Zubin P Olikara and Daniel J Scheeres. Numerical method for computing quasi-periodic orbits and their stability in the restricted three-body problem. *Advances in the Astronautical Sciences*, 145:911–930, 2012.
- 8) D.J. Scheeres. *Orbital Motion in Strongly Perturbed Environments : Applications to Asteroid, Comet and Planetary Satellite Orbiters*. Springer-Praxis, London (UK), 2012.
- 9) S. Van wal and D. J. Scheeres. The lift-off velocity on the surface of an arbitrary body. *Celestial Mechanics and Dynamical Astronomy*, 125(1):1–31, 2016.
- 10) G Voyatzis, I Gkolias, and H Varvoglis. The dynamics of the elliptic hill problem: periodic orbits and stability regions. *Celestial Mechanics and Dynamical Astronomy*, 113(1):125–139, 2012.
- 11) R.A. Werner and D.J. Scheeres. Exterior Gravitation of a Polyhedron Derived and Compared with Harmonic and Mascon Gravitation Representations of Asteroid 4769 Castalia. *Celestial Mechanics and Dynamical Astronomy*, 65:313–344, 1997.

- 12) W.E. Wiesel. Stable orbits about the martian moons. *Journal of Guidance Control Dynamics*, 16:434–440, 1993.
- 13) K Willner, J Oberst, H Hussmann, B Giese, H Hoffmann, K-D Matz, T Roatsch, and T Duxbury. Phobos control point network, rotation, and shape. *Earth and Planetary Science Letters*, 294(3):541–546, 2010.
- 14) K Willner, X Shi, and J Oberst. Phobos’ shape and topography models. *Planetary and Space Science*, 102:51–59, 2014.
- 15) Mattia Zamaro and JD Biggs. Natural motion around the martian moon phobos: the dynamical substitutes of the libration point orbits in an elliptic three-body problem with gravity harmonics. *Celestial Mechanics and Dynamical Astronomy*, 122(3):263–302, 2015.